Acta Crystallographica Section A
Foundations and Advances
ISSN 2053-2733

Received 14 May 2014
Accepted 31 October 2014

Nuclear-weighted X-ray maximum entropy method – NXMEM

Sebastian Christensen, Niels Bindzus, Mogens Christensen and Bo Brummerstedt Iversen*

Center for Materials Crystallography, Department of Chemistry and iNANO, Aarhus University, DK-8000 Aarhus, Denmark. Correspondence e-mail: bo@chem.au.dk

Subtle structural features such as disorder and anharmonic motion may be accurately characterized from nuclear density distributions (NDDs). As a viable alternative to neutron diffraction, this paper introduces a new approach named the nuclear-weighted X-ray maximum entropy method (NXMEM) for reconstructing pseudo NDDs. It calculates an electron-weighted nuclear density distribution (eNDD), exploiting that X-ray diffraction delivers data of superior quality, requires smaller sample volumes and has higher availability. NXMEM is tested on two widely different systems: PbTe and $Ba_8Ga_{16}Sn_{30}$. The first compound, PbTe, possesses a deceptively simple crystal structure on the macroscopic level that is unable to account for its excellent thermoelectric properties. The key mechanism involves local distortions, and the capability of NXMEM to probe this intriguing feature is established with simulated powder diffraction data. In the second compound, $Ba_8Ga_{16}Sn_{30}$, disorder among the Ba guest atoms is analysed with both experimental and simulated single-crystal diffraction data. In all cases, NXMEM outperforms the maximum entropy method by substantially enhancing the nuclear resolution. The induced improvements correlate with the amount of available data, rendering NXMEM especially powerful for powder and low-resolution single-crystal diffraction. The NXMEM procedure can be implemented in existing software and facilitates widespread characterization of disorder in functional materials.

1. Introduction

Exact knowledge of the atomic arrangement in functional materials is the foundation for understanding their physical properties. State-of-the-art data allow us to question even the most basic crystal structures. Supposedly simple structures might contain disorder, which plays a key role in the mechanisms governing the excellent thermoelectric properties of these materials (Bozin *et al.*, 2010; Kastbjerg *et al.*, 2013; Knox *et al.*, 2014). The atomic structure is a prerequisite for performing accurate theoretical calculations, and local symmetry dictates the selection rules for Raman and IR spectroscopy. Therefore, experimental data risk being misinterpreted if only analysed in view of the average crystal structure.

The maximum entropy method (MEM) presents itself as an ideal method to analyse crystal structures featuring unanticipated features, as it offers model-independent estimations of electron-density distributions (EDDs) (Collins, 1982; Sakata & Sato, 1990). Using Bayesian statistics, the EDD is inferred in a logically consistent manner from a limited set of structure factors, F_{obs}. The MEM reconstruction directly implements the experimental data, rendering it sensitive to systematic errors (Cargnoni *et al.*, 2004). Within the field of crystallography, MEM has been applied to assess chemical bonding and atomic charges, calculation of electrostatic potentials, and structural characterization of disorder and anharmonic vibrations (Bentien *et al.*, 2002; Snyder *et al.*, 2004; Nishimura *et al.*, 2008; Bindzus & Iversen, 2012; Tanaka *et al.*, 2006).

To aid in the analysis of structural disorder and anharmonic motion, we introduce a novel method called the nuclear-weighted X-ray maximum entropy method (NXMEM). The objective of NXMEM is to recover a quantity with the same spatial distribution as the nuclear density distributions (NDDs) from a limited set of X-ray structure factors. The NDD is desirable owing to its sharper atomic features compared with the equivalent EDD. This enhanced resolution may be vital for resolving closely spaced features. Information about the NDD is conventionally obtained from neutron diffraction (Takata *et al.*, 1994), which leads to a scattering-length-weighted NDD. Similarly, with NXMEM we obtain an electron-weighted nuclear density distribution (eNDD). Consequently, heavier atoms will also be more prominent in the eNDD. Synchrotron X-ray data collected in a few minutes are in general statistically superior to neutron diffraction data collected over several hours. This makes it appealing to extract pseudo NDDs from X-ray structure factors.

NXMEM is tested on two widely different systems, PbTe and $Ba_8Ga_{16}Sn_{30}$ (Fig. 1), benchmarking its performance

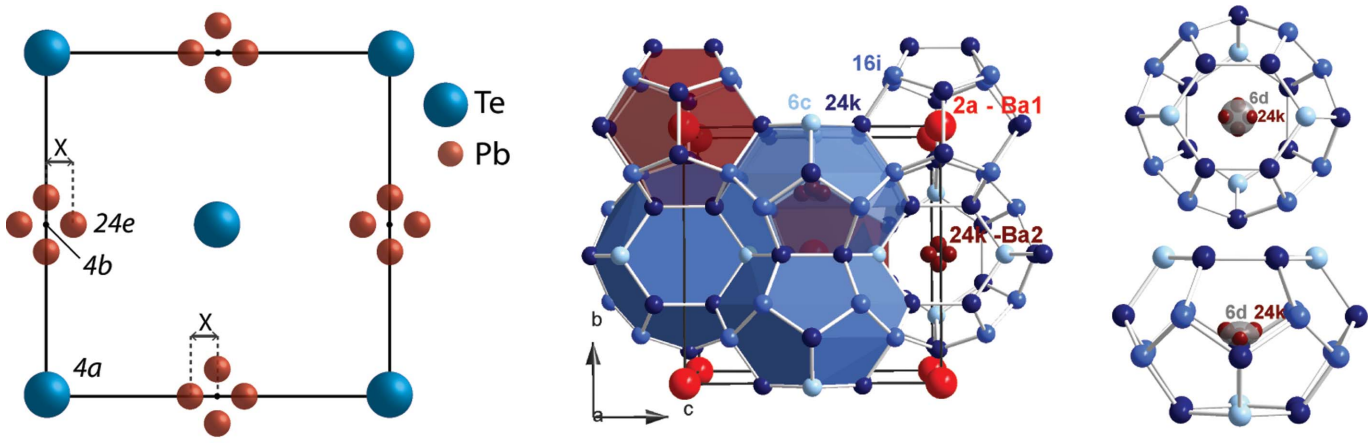

(*a*) (*b*) (*c*)

Figure 1
(*a*) The disordered rock salt structure of PbTe. Pb is displaced by *x* in the equivalent ⟨100⟩ directions away from the 4*b* site to the 24*e* site. (*b*) The type-I clathrate structure of $Ba_8Ga_{16}Sn_{30}$. The host structure is built from Ga and Sn, which share the blue sites. The host structure forms cages which contain the Ba guest atoms: Ba1 on the 2*a* site and Ba2 partially occupying the 24*k* sites around the 6*d* site. (*c*) Ba is placed on the 24*k* site in the simulated data, while the simplistic refinement model places Ba2 on the 6*d* site and allows the disorder to be absorbed into the anisotropic thermal parameters.

against standard MEM. In both systems, the understanding of disorder is vital to explain their physical properties. Firstly, NXMEM is tested on purely simulated powder X-ray diffraction (PXRD) data based on PbTe. Secondly, NXMEM is applied to both experimental and simulated single-crystal X-ray diffraction (SCXRD) data on the structurally complex type 1 clathrate $Ba_8Ga_{16}Sn_{30}$. The two types of investigated data pose different challenges to the MEM and NXMEM reconstructions as the treatment of the PXRD data is inherently more complicated. Of particular importance are the weaker data constraints obtained by PXRD.

PbTe displays a deceptively simple crystal structure on the macroscopic level; however, Bozin *et al.* (2010) presented evidence from neutron PDF (pair distribution function) data that Pb is locally displaced along the 100 directions away from its high-symmetry site (Fig. 1*a*). This was subsequently confirmed by MEM analysis of synchrotron PXRD data (Kastbjerg *et al.*, 2013). Despite the efforts of these studies, the true nature of the Pb distortion remains a controversial topic with opposing descriptions based on abnormal anharmonic effects or subtle disorder (Keiber *et al.*, 2013; Zhang *et al.*, 2011). A key reason for this uncertainty is the achieved direct-space resolution, which is insufficient to clearly identify whether off-centred maxima emerge in the Pb distribution. It is therefore essential to further probe this intriguing phenomenon to properly elucidate the true origin of the low thermal conductivity in PbTe and related compounds. To test the sensitivity of MEM and NXMEM, we applied the methods to simulated PXRD data of PbTe structures with increasing Pb displacements.

The intermetallic type-I clathrates have been extensively studied owing to their thermoelectric properties (Christensen *et al.*, 2010). Group 13 and 14 elements form a host structure framework with cages filled by guest atoms of group 1 or 2 elements (Fig. 1*b*). The guest atoms have been linked to the unusually low thermal conductivity (Nolas *et al.*, 1998). Therefore, their spatial distribution has been intensely studied with X-ray and neutron diffraction (Bentien *et al.*, 2000, 2002; Sales *et al.*, 2001; Christensen *et al.*, 2006). In the current study, NXMEM has been applied to SCXRD data collected at 100 K and 300 K (Christensen *et al.*, 2013). The obtained NXMEM results are further validated by application to simulated data.

This paper explains the basic concept of NXMEM and how these calculations can be performed by modifying the input to existing MEM software like *BayMEM* (van Smaalen *et al.*, 2003). As proof of concept, NXMEM is validated against simulated and experimental data of PbTe and $Ba_8Ga_{16}Sn_{30}$. Both cases establish that NXMEM is superior to MEM in terms of resolving and quantifying subtle disorder.

2. The concept of NXMEM

The difference between MEM and NXMEM is schematically illustrated in Fig. 2. Both methods start by refining SCXRD or PXRD data to obtain phased structure factors, $F_{\rm obs}^{\rm EDD}(\mathbf{H})$, that are absolutely scaled and corrected for anomalous dispersion, extinction and absorption; $\mathbf{H}$ represents the reciprocal-lattice vector (Bindzus & Iversen, 2012). In the MEM analysis, the $F_{\rm obs}^{\rm EDD}(\mathbf{H})$'s are fed directly into the MEM algorithm and the output is the EDD of the unit cell. NXMEM introduces an additional step, which transforms all $F_{\rm obs}^{\rm EDD}(\mathbf{H})$ into nuclear structure factors, $F_{\rm obs}^{\rm eNDD}(\mathbf{H})$, by normalization to the atomic form factors, $f_j(H)$. The nuclear scattering is hereby mimicked by eliminating the angular decay in scattering power caused by the diffuse distribution of electrons. By using the $F_{\rm obs}^{\rm eNDD}(\mathbf{H})$'s for MEM, we obtain the electron-weighted nuclear density distribution (eNDD). In other words, NXMEM deconvolutes the EDD in reciprocal space to obtain the eNDD. A full account of the normalization procedure follows below.

Below we write the X-ray structure factor as a sum of partial structure factors, $F_{{\rm model},j}^{\rm EDD}$, over the different elements, *j*. Within the independent atom model (IAM) approximation, $F_{{\rm model},j}^{\rm EDD}$ is

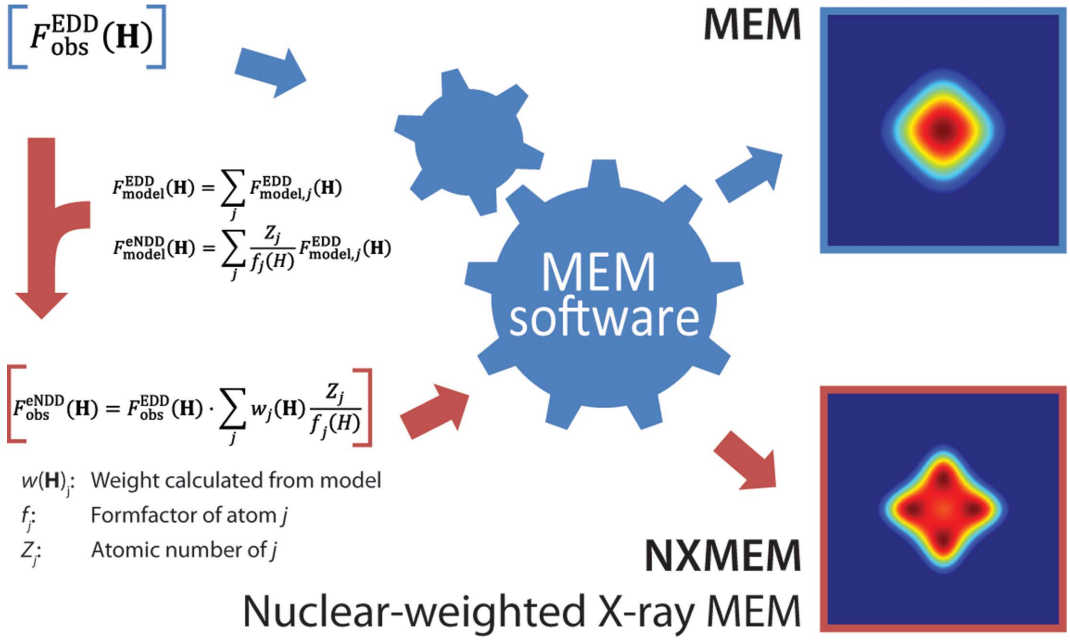

Figure 2
Schematic illustration of the difference between MEM (top in blue) and NXMEM (bottom in red). After the experimental extraction of F_{obs}^{EDD}, NXMEM introduces an additional step to calculate nuclear structure factors, F_{obs}^{eNDD}. MEM software transforms these into the eNDD, thereby resolving multiple maxima which are hidden in the EDD obtained by MEM.

the contribution of a single element with form factor, f_j, to the total structure factor, F_{model}^{EDD}:

$$F_{model,j}^{EDD}(\mathbf{H}) = f_j(H) \sum_i \exp(i2\pi \mathbf{r}_i \cdot \mathbf{H}) T_i(\mathbf{H}),$$
$$F_{model}^{EDD}(\mathbf{H}) = \sum_j F_{model,j}^{EDD}(\mathbf{H}), \quad (1)$$

where r_i and T_i are the position and temperature factor of the ith atom of element j. If for each atom we imagine that all its electrons are assembled at the nucleus, an electron-weighted nuclear structure factor can be formulated by substituting f_j with the atomic number, Z_j:

$$F_{model,j}^{eNDD}(\mathbf{H}) = Z_j \sum_i \exp(i2\pi \mathbf{r}_i \cdot \mathbf{H}) T_i(\mathbf{H}) = \frac{Z_j}{f_j(H)} F_{model,j}^{EDD}(\mathbf{H}),$$
$$F_{model}^{eNDD}(\mathbf{H}) = \sum_j F_{model,j}^{eNDD}(\mathbf{H}) = \sum_j \frac{Z_j}{f_j(H)} F_{model,j}^{EDD}(\mathbf{H}). \quad (2)$$

The Fourier transform of F^{eNDD} is then the eNDD. The fundamental assumption of NXMEM is that F_{obs}^{eNDD} can be calculated from F_{obs}^{EDD} by multiplication with a deconvolution factor, df:

$$F_{obs}^{eNDD}(\mathbf{H}) = F_{obs}^{EDD}(\mathbf{H}) \times df(\mathbf{H}). \quad (3)$$

The standard deviations of $F_{obs}^{EDD}(\mathbf{H})$ are also multiplied by the same factor in order to preserve the significance distribution. Therefore, NXMEM is not a weighting scheme as previously applied to MEM calculations (de Vries *et al.*, 1994; Iversen *et al.*, 1995). By employing the best structural model, df is calculated as

$$df(\mathbf{H}) = \frac{F_{model}^{eNDD}(\mathbf{H})}{F_{model}^{EDD}(\mathbf{H})} = \sum_j w_j(\mathbf{H}) \frac{Z_j}{f_j(H)},$$
$$\text{where } w_j(\mathbf{H}) = \frac{F_{model,j}^{EDD}(\mathbf{H})}{F_{model}^{EDD}(\mathbf{H})}. \quad (4)$$

The weight factor, w_j, measures the contribution of the element j to the total structure factor. From the equations above, one can infer that NXMEM becomes exact for: (i) monoatomic compounds, (ii) the hypothetical case where the form factors of different elements have identical angular dependence, $f_k(\mathbf{H})/Z_k = f_l(\mathbf{H})/Z_l$, $k \neq l$, and (iii) if the structural model is true, $F_{obs}^{EDD}(\mathbf{H}) = F_{model}^{EDD}(\mathbf{H})$. Other possible formulations of the deconvolution factor were tested but rejected due to artefacts in the resulting eNDDs (see the supporting information for more details[1]).

The NXMEM procedure resembles well known methods of both X-ray total scattering and structure solution. In total scattering the Morningstar–Warren approximation is employed to promote internuclear distances (Warren *et al.*, 1936; Egami & Billinge, 2003). Patterson also used normalized intensities to sharpen peaks in Patterson maps (Patterson, 1935). Direct structure-solution methods employ normalized structure factors to impose atomic discreteness (Hauptman, 1986). In both cases the scattering function and structure factors are normalized to the form factors based only on the elemental composition. In contrast, NXMEM uses the *best* known structural model to optimally normalize each F_{obs}^{EDD}.

NXMEM is a general concept, which is applicable in other contexts that can benefit from deconvolution from the atomic

[1] Supporting information for this article is available from the IUCr electronic archives (Reference: IB5029).

Table 1
Parameters and agreement factors for refinement against the series of PbTe data sets simulated at the 100 K conditions.

All agreement factors are defined in Bindzus & Iversen (2012).

	x				
	0.00	0.01	0.02	0.03	0.04
R_{obs}/wR_{obs} ($I > 3\sigma$) (%)	0.21/0.27	0.18/0.25	0.56/0.78	1.91/1.78	6.63/6.19
R_{all}/wR_{all} (%)	0.21/0.27	0.21/0.26	0.66/0.80	2.38/1.85	7.00/6.22
R_p/wR_p (%)	0.36/0.47	0.36/0.47	0.37/0.49	0.48/0.62	0.78/1.15
χ^2	0.34	0.33	0.34	0.43	0.78
U_{iso}(Pb) (Å^2)	0.00530 (8)	0.00668 (9)	0.01103 (1)	0.01859 (2)	0.03044 (6)
U_{iso}(Te) (Å^2)	0.00528 (1)	0.00532 (1)	0.00545 (2)	0.00596 (2)	0.00617 (4)

electron distribution. At the fundamental level, the definition of NXMEM is to include a deconvolution step in the MEM Fourier reconstruction. One could equally well attempt to go even further and deconvolute thermal motion to obtain a pseudo static eNDD.

Despite the approximating nature of NXMEM, the test cases presented in the next sections reveal that NXMEM recovers the true structures even when employing simplistic models for the normalization, and the extraction and phasing of structure factors.

3. Technical details

3.1. PbTe PXRD simulation

Inspired by the proposed disorder in PbTe (Bozin *et al.*, 2010), the performance of NXMEM is evaluated against simulated PXRD data of PbTe ($Fm\overline{3}m$, a = 6.435 Å) with increasing degrees of disorder. In the test structures, Pb is systematically displaced from the 4*b* position at (0.5, 0.5, 0.5) to the surrounding 24*e* positions at $(0.5 + x, 0.5, 0.5)$, $x = 0, 0.01, 0.02, 0.03, 0.04$ (Fig. 1*a*). Te is maintained at the 4*a* position (0, 0, 0). Note that these simulations do not imply anything about the controversial features of real PbTe. They are simply used to quantify how small displacements are resolvable with MEM and NXMEM.

To mimic experimentally attainable data quality, we chose the $\sin(\theta)/\lambda$ resolution, isotropic atomic displacement parameters and peak-shape parameters in accordance with actual data collected at beamline BL44B2, SPring-8 using λ = 0.50007 Å:

$$T = 100\ \text{K}:\ \sin(\theta)/\lambda = 1.20\ \text{Å}^{-1},\ U_{iso}(\text{Te}) = U_{iso}(\text{Pb}) = 0.0053\ \text{Å}^2,$$
$$T = 300\ \text{K}:\ \sin(\theta)/\lambda = 1.07\ \text{Å}^{-1},\ U_{iso}(\text{Te}) = U_{iso}(\text{Pb}) = 0.014\ \text{Å}^2.$$

In the interest of simplicity and direct comparison of the Pb displacements, the lattice parameters are kept identical at both temperatures. Simulated powder diffraction patterns, $I_{calc}(2\theta)$, were calculated on a constant background by *JANA2006* (Petříček *et al.*, 2014). These simulations do not include anomalous dispersion, and Gaussian noise was added before reimporting them into *JANA2006*. The simulated data were refined against a simplistic model where Pb and Te are positioned on high-symmetry positions: Pb on 4*b* (0.5, 0.5, 0.5) and Te at 4*a* (0, 0, 0). Both atoms had a single parameter to model isotropic thermal motion: U_{iso}(Pb) and U_{iso}(Te). This approach results in a total of 12 adjustable parameters. Most importantly, it imposes minimal model bias towards a disordered Pb during the extraction of structure factors. The results of the refinements against the 100 K data are shown in Table 1. The monotonically increasing U_{iso}(Pb) reflects progressively stronger Pb displacements. All parameters for the model and refined structures are reported in the supporting information. The standard deviations of observed structure factors, $\sigma_{obs}^{EDD}(\mathbf{H})$, were estimated by the 'profile fitting' option in *JANA2006*.

3.2. $Ba_8Ga_{16}Sn_{30}$

Details of data collection on $Ba_8Ga_{16}Sn_{30}$ are reported in Christensen *et al.* (2013). In addition, based on the '24k-model' from the same study, we simulated data sets at 100 K and 300 K with coverage and standard deviations identical to the experimental data.

All data were refined in *JANA2006* using a simplistic, ordered model (Table 2). All atoms are described by anisotropic atomic displacement parameters, and the guest atom in the large cage; Ba2 is placed in the cage centre on the 6*d* site (0.25, 0.5, 0) (Fig. 1*c*). This structural model does therefore not introduce any prior bias towards anharmonic motion or disorder of Ba2. The refinement procedure and constraints are fully described in Christensen *et al.* (2013).

MEM and NXMEM calculations were performed on the full simulated and experimental data sets, $\sin(\theta)/\lambda|_{max}$ = 1.06 Å^{-1}. In addition, the same data were analysed with an angular cut-off, excluding all data above $\sin(\theta)/\lambda$ = 0.4 Å^{-1}.

3.3. MEM reconstruction

All MEM calculations were performed using *BayMEM* (van Smaalen *et al.*, 2003). The grid size was 256^3, giving a voxel size of $(0.025\ \text{Å})^3$ for PbTe and $(0.046\ \text{Å})^3$ for

Table 2
Details of data collection and refinement against $Ba_8Ga_{16}Sn_{30}$ X-ray data simulated and collected at 100 K and 300 K.

Definitions of agreement factors are given by Bindzus & Iversen (2012). All refined parameters are reported in the supporting information.

	Simulation		Experimental	
Temperature (K)	100	300	100	300
N_{par}	17	17	18	18
N_{obs}	1452	1464	1452	1464
N_{obs} ($I > 3\sigma$)	1099	922	1130	938
R_F/wR_F (%)	7.52/9.04	7.08/6.20	7.31/9.22	6.61/6.35
R_F/wR_F ($I > 3\sigma$) (%)	5.85/8.94	4.21/5.96	6.02/8.92	4.16/5.62
$R_{internal}$ (%)			3.9	4.41
Ba2 6*d*				
U_{11} (Å^2)	0.031 (2)	0.047 (1)	0.016 (1)	0.0332 (10)
U_{22} (Å^2)	0.205 (4)	0.188 (2)	0.220 (4)	0.202 (2)

Table 3
The relative position of the density maximum, x_{max}, and centre-of-charge, x_{coc}, determined by *EDMA*.

The agreement with the true value is expressed by the relative deviation: $\Delta x/x = (x_{max,coc} - x_{model})/x_{model}$.

		100 K				300 K			
	x_{model}	x_{max}	$\Delta x/x$	x_{coc}	$\Delta x/x$	x_{max}	$\Delta x/x$	x_{coc}	$\Delta x/x$
NXMEM	0.03	0.0277	−7.65%	0.0298	−0.57%				
	0.04	0.0504	25.98%	0.0415	3.78%	0.0380	−0.1	0.0416	0.0
MEM	0.04	0.0115	−71.32%	0.0588	47.07%				

$Ba_8Ga_{16}Sn_{30}$. The order of the generalized F and G constraints was the standard value of 2 and no *ad hoc* weighting scheme was employed (de Vries *et al.*, 1994; Iversen *et al.*, 1995). The Lagrange multiplier was initially set to 10^{-4}, but automatically adjusted in subsequent cycles. To enforce minimal model bias, calculations were started from uniform prior EDDs/eNDDs. The only exception was the PbTe, 100 K, $x = 0.04$ MEM reconstruction where divergence issues were resolved with a non-uniform prior EDD based on the refined model.

The program *PRIOR* was used to calculate EDDs and eNDDs from model structures (van Smaalen *et al.*, 2003). The standard usage of *PRIOR* is to calculate EDDs; however, the supporting information describes how it can easily be extended to eNDDs. Simple topological analysis of the EDD/eNDDs was performed by *EDMA* (Palatinus *et al.*, 2012).

The expectation value for the MEM stopping criterion is $\chi^2 = 1$; however, this is not necessarily the optimal value (Hofmann *et al.*, 2007; Bindzus & Iversen, 2012). In the present paper, we study the MEM and NXMEM densities at multiple χ^2 values. Calculations were continued until stagnation of χ^2, while saving the progress of the MEM iteration at multiple preselected values. Hofmann *et al.* (2007) proposed that an optimum value of χ^2 should be chosen, for which apparent structure features in the difference Fourier density, ρ_{FD}, have reached the noise level. The ambiguity of this method arises from selection of the most representative crystal planes and from difficulties in distinguishing between noise and structure regions. To address these issues, Bindzus & Iversen (2012) suggested using a residual density analysis scheme which takes the entire ρ_{FD} into account. We applied both methods to the data and found that visual inspection of ρ_{FD} maps best avoided overfitting and produced the smoothest densities. The optimum stopping criteria for the presented MEM maps were therefore determined by this method. Further details are given in the supporting information.

For PXRD data, application of G constraints is crucial for reducing bias towards an ordered structure since overlapping reflections are decomposed based on the simplistic Rietveld model. G constraints resolve this by implementing groups of overlapping Bragg peaks as single intensities in the MEM reconstruction (Sakata *et al.*, 1990). For example, at 100 K the 132 observed structure factors were reduced to 29 F_{obs} and 33 G_{obs} due to peak overlap. The grouped reflections, G_{obs}, include all cases displaying partial or complete overlap, *e.g.* 115/333.

Fig. 3 provides an overview of the NXMEM procedure used in the present study. Steps (*a*)–(*c*) are done using *JANA2006*, steps (*d*)–(*e*) have been automated using *MATLAB* scripts (Mathworks, 2010), and step (*f*) is performed by *BayMEM*. See the supporting information for an extended description of each step.

a) Refine experimental X-ray diffraction data
b) Extract correctly scaled and corrected observed structure factors, $F(\mathbf{H})^{EDD}_{obs}$
c) Calculate partial structure factors, $F(\mathbf{H})^{EDD}_{model,j}$, based on the refined model
d) Calculate $F(\mathbf{H})^{eNDD}_{obs}$ using equation (3) and (4)
e) Identify strongly overlapping reflections and calculate group intensities, $G(\mathbf{H_1}, \mathbf{H_2}, \ldots)^{eNDD}_{obs}$
f) MEM reconstruction of eNND using $F(\mathbf{H})^{eNDD}_{obs}$ and $G(\mathbf{H})^{eNDD}_{obs}$ as data input

Figure 3
Outline of the present NXMEM procedure.

4. Results

4.1. PbTe

The spatial distribution of the 100 K eNDDs calculated by NXMEM is shown in Fig. 4 (top) for the Pb site. As a reference, we also calculated the true eNDD from the actual model structures using *PRIOR* (Fig. 4, bottom). For $x = 0$ and 0.01 (0.064 Å), the eNDD of Pb is spherical and there is no evidence of disorder (Fig. 4, top). In contrast, Pb is clearly displaced away from the 4*b* position for x = 0.03 (0.19 Å) and 0.04 (0.26 Å). The position of the NXMEM density maximum, x_{max}, is listed in Table 3 together with its deviations from the true value. The centre-of-charge, x_{coc}, *i.e.* the first moment of the charge distribution, is also included in Table 3. It appears to be a much more reliable measure of the displacement, deviating by less than 5% from the true values. Furthermore, x_{coc} is much less sensitive to the choice of χ^2. The NXMEM density for $x = 0.02$ is an intermediate case. There are no off-centre maxima, but the eNDD is clearly aspherically distorted in the directions of the Pb displacement. Note that the combined effect of finite data resolution and loose data constraint smears the NXMEM eNDD compared with the reference eNDD. An equivalent analysis of the 300 K NXMEM calculations is presented in the supporting information together with the NXMEM eNDD of Te. In general, the Te density experiences negligible distortions and disorder effects are unequivocally assigned to Pb. For $x = 0.04$, the Te density develops a minimum at the 4*a* site in disagreement with the true structure. This artefact arises from inconsistencies in the extracted F^{EDD}_{obs} and is resolved by using a non-uniform prior density based on the refinement model.

To highlight the advantages of NXMEM over MEM, we performed MEM calculations directly on $F^{EDD}_{obs}(\mathbf{H})$ to obtain the EDD shown in Fig. 5. For x = 0, 0.01 and 0.02, the density distribution around the Pb position remains unsuggestive of any disorder. For $x = 0.03$, an aspherical distortion emerges; however, the EDD maximum remains at the 4*b* position (Fig.

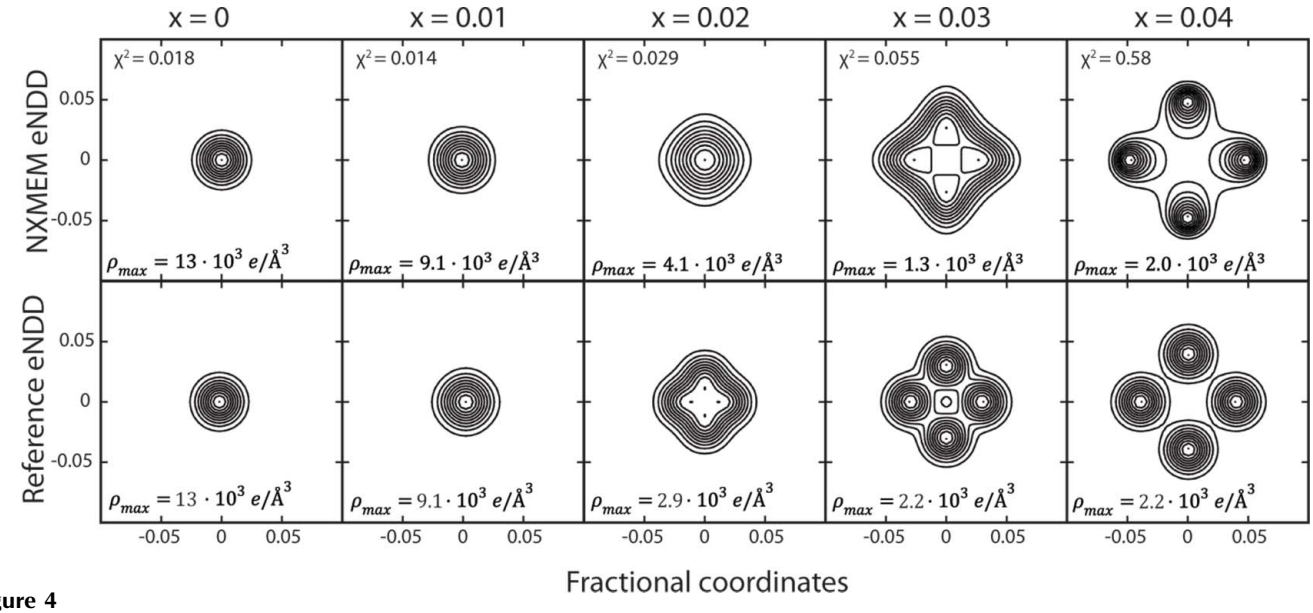

Figure 4
(Top) NXMEM NDDs of Pb in the (001) plane through the 4*b* position. (Bottom) Reference NDDs calculated from the true structure. Contour lines are drawn in steps of $\rho_{max}/10$, where ρ_{max} is the maximum density of the map in question.

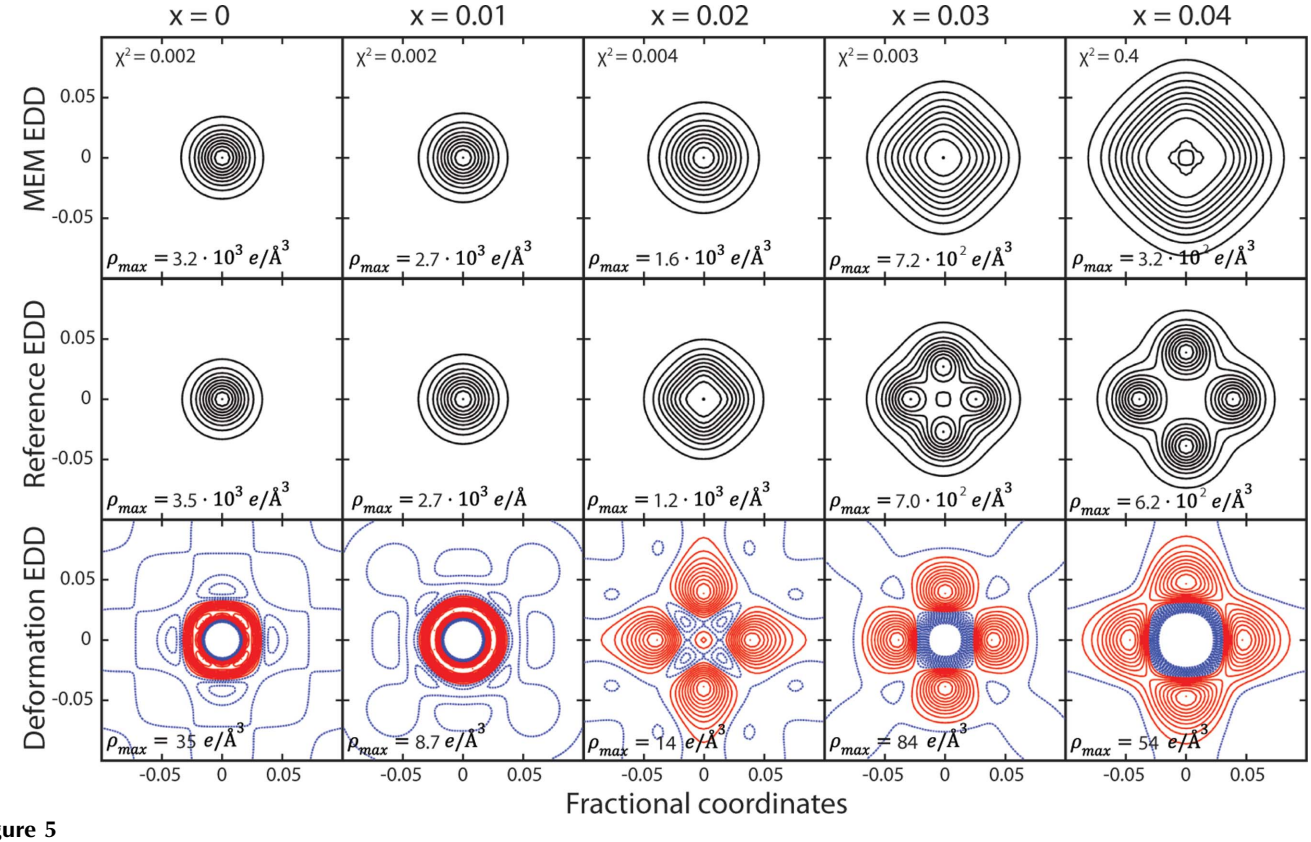

Figure 5
(Top) MEM EDDs of Pb in the (001) plane through the 4*b* position. (Middle) Reference EDDs calculated from the true structure. Contour lines are drawn in steps of $\rho_{max}/10$, where ρ_{max} is the maximum density of the map. (Bottom) Deformation densities defined by $\rho_{deform}(\mathbf{r}) = \rho_{MEM}(\mathbf{r}) - \rho_{model}(\mathbf{r})$. Contour lines are drawn in steps of $\rho_{max}/10$ in the interval $[-\rho_{max}, \rho_{max}]$. Positive (red) and negative contours (blue).

5, top row). In contrast, the corresponding reference density clearly reveals off-centred Pb atoms. Only for $x = 0.04$ do off-centre maxima become visible; however, they are poorly defined with substantial errors in their maximum position and centre-of-charge of 71% and 47% (Table 3).

Previous studies have probed disorder features by deformation densities, $\rho_{deform}(\mathbf{r}) = \rho_{MEM}(\mathbf{r}) - \rho_{model}(\mathbf{r})$ (Bentien *et al.*, 2002; Kastbjerg *et al.*, 2013). $\rho_{MEM}(\mathbf{r})$ and $\rho_{model}(\mathbf{r})$ are the EDDs calculated by MEM and from the ordered model, respectively. Employing this approach for the present simu-

lations reveals maxima along the directions of the Pb displacement for $x = 0.02, 0.03, 0.04$ (Fig. 5, bottom row). However, the maximum positions substantially overestimate the actual Pb offset by 95%, 30% and 18%. This demonstrates that the displacement distance obtained from deformation densities merely approaches the correct value for large displacements. This observation implies why MEM-derived deformation densities lead to substantially larger Pb off-centring compared with neutron PDF data (Bozin *et al.*, 2010; Kastbjerg *et al.*, 2013).

4.2. $Ba_8Ga_{16}Sn_{30}$

Fig. 6 shows isosurface plots of the NXMEM eNDD for the entire unit cell viewed along the *a* direction for both simulated and experimental data at 100 K. The disorder of Ba2 is clearly observed in both cases. Importantly, in accordance with previous work none of the other atoms show signs of disorder (Christensen *et al.*, 2013). To analyse the Ba2 distribution more carefully, we calculate contour maps of the (001) and (100) planes for the simulated (Fig. 7) and the experimental (Fig. 8) data set.

First we focus on the simulated data in Fig. 7. For the full data set the disorder positions are resolved at 100 K and 300 K for both NXMEM and MEM (Figs. 7*a*,*b*). The features are more localized for NXMEM; however, this slight improvement augments only the quantitative description of the disorder. Considering the displacement from the 6*d* site, Table 4 shows that the distances estimated by NXMEM are consistently more accurate. If the resolution of the data is reduced to $\sin(\theta)/\lambda = 0.4$ Å^{-1}, the advantage of NXMEM becomes apparent (Figs. 7*c*,*d*). Although the density is smeared due to the data cutoff, NXMEM manages to resolve the disorder position and determine the displacement distance within 6% in both cases (Fig. 7*c* and Table 4). In contrast, any proof of disorder has vanished in the MEM EDD as it merely shows minute off-centre maxima at 100 K and 300 K (Fig. 7*d*).

Table 4
The fractional distance from 6*d* to the centre-of-charge of density maxima at 24*k*, d_{6d-24k}, has been determined for simulated data by *EDMA*.

The agreement with the true atomic displacement distance is expressed by the relative difference: $\Delta d/d^{\rm model} = (d^{\rm NXMEM}_{6d-24k} - d^{\rm model}_{6d-24k})/d^{\rm model}_{6d-24k}$.

	100 K		300 K	
	d_{6d-24k}	$\Delta d/d^{\rm model}$ (%)	d_{6d-24k}	$\Delta d/d^{\rm model}$ (%)
Model	0.0411		0.0380	
NXMEM				
Full data set	0.0412	0.24	0.0387	−6.0
Low resolution	0.0409	−0.51	0.0391	−4.8
MEM				
Full data set	0.0439	6.6	0.0430	4.5
Low resolution	0.0446	8.5	0	−100

Having seen NXMEM work satisfactorily on simulated data, we move on to testing it against experimental data. Starting with the full data set at 100 K, we see that the density maximum is clearly displaced from the 6*d* site (Fig. 8*a*). In contrast to the simulated '24k-model', Ba2 does not appear to be spherically distributed around the 24*k* sites. Instead, it is continuously distributed around a torus with maximal densities at the 24*k* sites. Comparing the results at 100 K and 300 K, the nuclear enhancement introduced by NXMEM is vital for resolving the disorder in the complete temperature range. Even though MEM recovers the true disorder picture at 100 K, it fails at 300 K (Fig. 8*b*). Furthermore, at both temperatures the MEM densities appear jagged and thus overfitted. As in the simulated example, the superior performance of NXMEM becomes more pronounced if the data resolution is lowered to $\sin(\theta)/\lambda = 0.4$ Å^{-1}. Even in this challenging case NXMEM manages to correctly resolve the Ba2 disorder at 100 K, while only weak off-centre maxima emerge at 300 K (Fig. 8*c*). In contrast, the disorder remains concealed at 300 K and barely resolved at 100 K if the analysis is based on conventional MEM calculations (Fig. 8*d*).

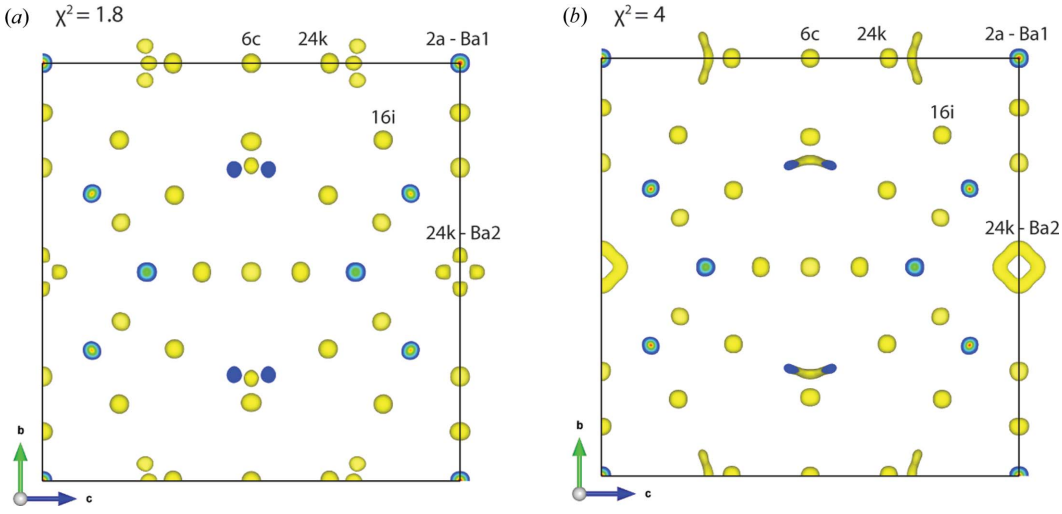

Figure 6
Isosurface plot of the eNDD of $Ba_8Ga_{16}Sn_{30}$ at 100 K for the (*a*) simulated and (*b*) experimental data set. The disordered Ba2 guest atom can be identified as (*a*) the four closely spaced spheres and as (*b*) the torus-shaped object. All other atoms remain approximately spherical. Isosurface: 70 e Å^{-3}.

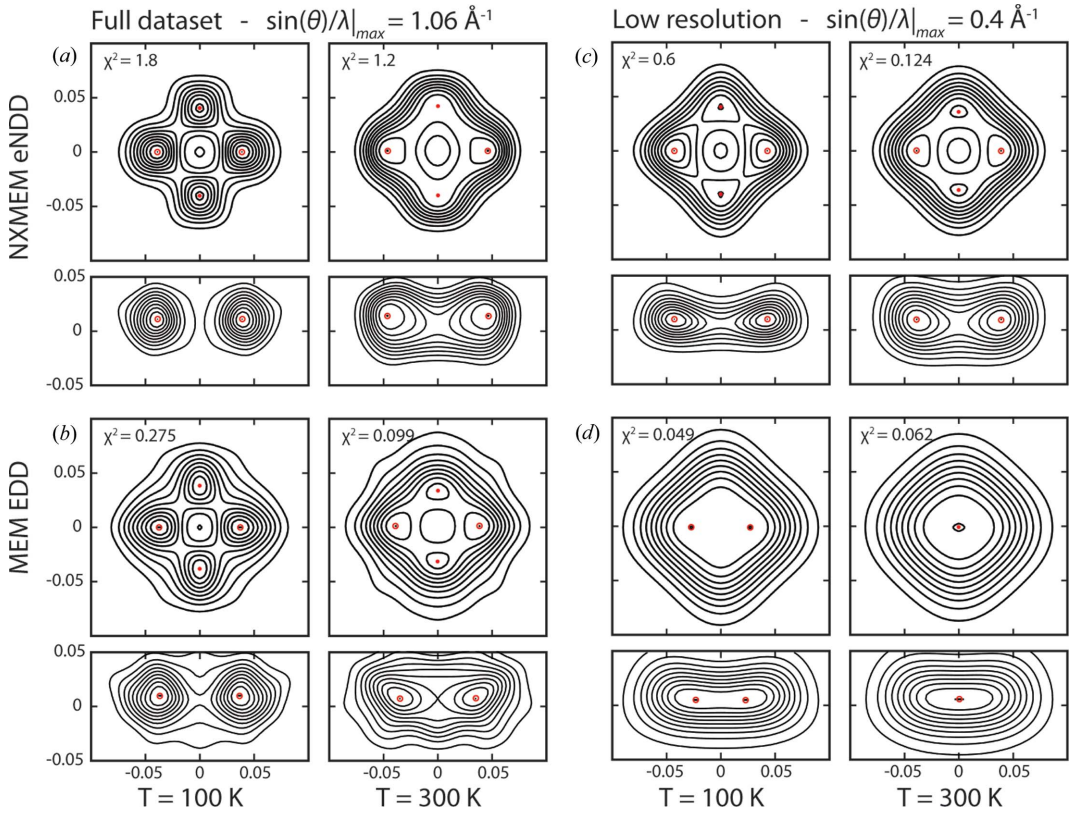

Figure 7
Simulation: the eNDD and EDD around the Ba2 position obtained from simulated data using (*a*), (*c*) NXMEM and (*b*), (*d*) MEM. The top and bottom subfigures show the (100) and (001) planes, respectively. Both are centred on (0.244, 0.5, 0). Local maxima are marked in red.

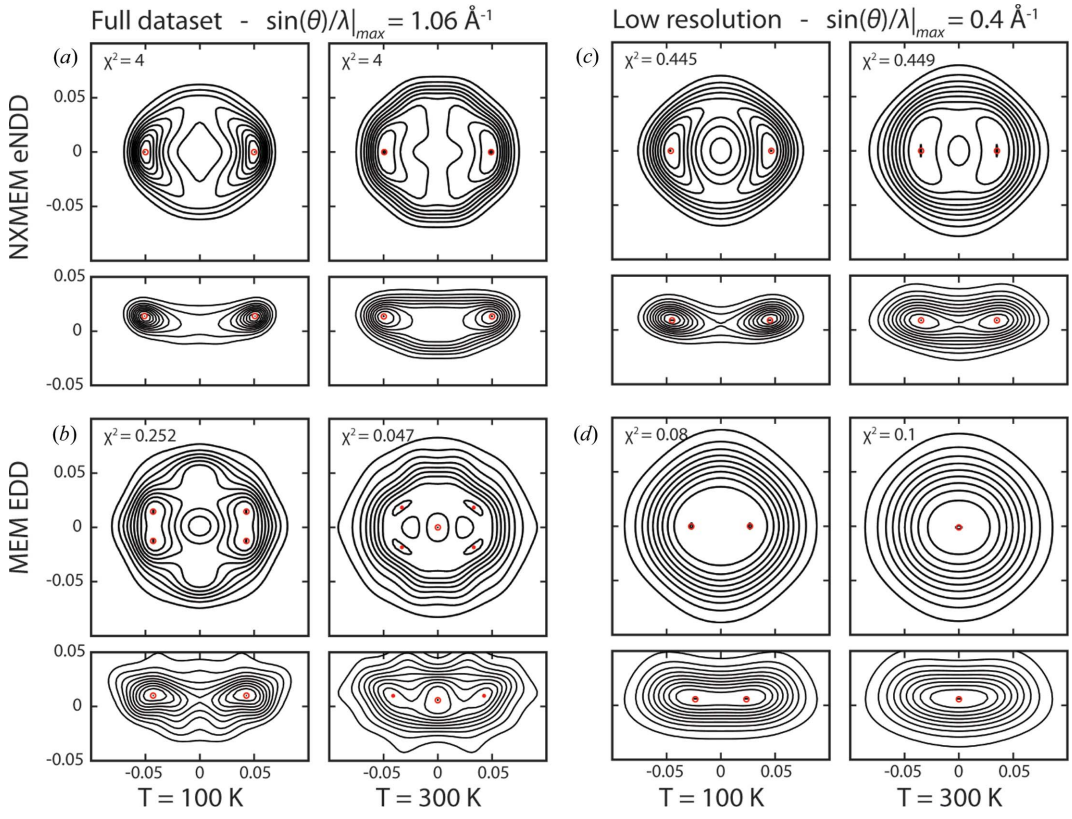

Figure 8
Experimental: the eNDD/EDD around the Ba2 position obtained from experimental data using (*a*), (*c*) NXMEM and (*b*), (*d*) MEM. The top and bottom subfigures show the (100) and (001) planes, respectively. Both are centred on (0.244, 0.5, 0). Local maxima are marked in red.

5. Discussion

In the previous section, it was established that NXMEM outperforms MEM in terms of resolving and quantifying the Pb and Ba displacements. However, it is difficult to quantify how much NXMEM improves the nuclear resolution. At 100 K PbTe, the smallest displacement resolved by NXMEM is $x = 0.03$ (0.19 Å), which is 25% smaller compared to the displacement resolved by MEM, $x = 0.04$ (0.26 Å). Since MEM severely underestimates the displacement at $x = 0.04$, the numbers are not directly comparable. Similar improvements are observed when NXMEM is applied to simulated and experimental low-resolution data of $Ba_8Ga_{16}Sn_{30}$, where it clearly outperforms MEM in the characterization of the disordered Ba atom. When the full data set is used the advantage of NXMEM is more subtle, but in the experimental case only NXMEM is capable of resolving the disorder at 300 K.

We believe there are two contributions to the increased resolution of NXMEM compared to MEM: (i) NXMEM performs a reciprocal-space deconvolution of the EDD, leading to the eNDD and thus sharper atomic features. Hereby, it reduces overlap of closely spaced peaks. However, if one compares the reference EDD of the model structure with the eNDD (see Fig. 9), it is evident that the effect of convoluting with the atomic electron distribution is only minor in the high-density region. Thus, if MEM was able to obtain the true EDD it would, for example, resolve the displacement of Pb at $x = 0.03$. However, this is not the case, which leads to the second contribution. (ii) NXMEM emphasizes the discreteness of atoms that form the electron density, *i.e.* atomicity (Hauptman, 1986; Giacovazzo, 2002). Compared with MEM, it therefore has a different and more restrictive solution space, which only covers the most localized density maps. In consequence, the NXMEM procedure is less sensitive to the amount of experimental data. This key property renders the usage of NXMEM beneficial especially for PXRD and low-resolution single-crystal diffraction.

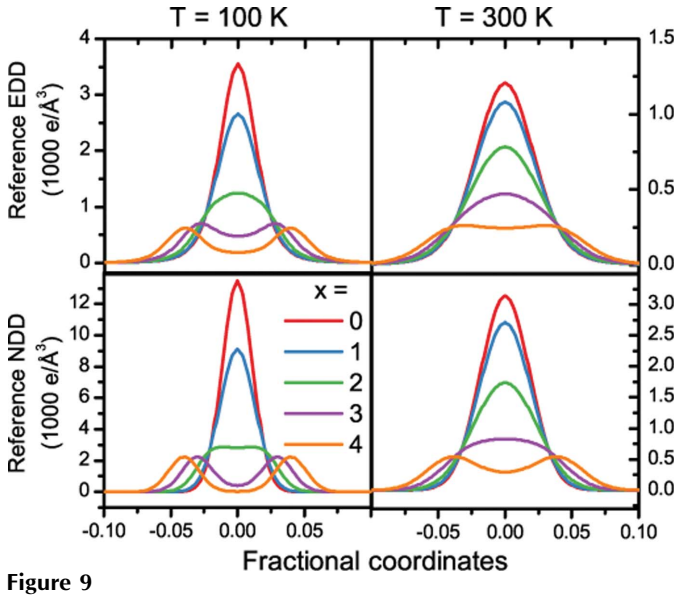

Figure 9
Cross section through the Pb position of the true reference EDD (top) and eNDD (bottom). The atomic features are slightly narrower and thus higher in the eNDD.

In both MEM and NXMEM, overfitting of data can introduce artefacts in the density. Of the presented test cases, this problem was most pronounced for the SCXRD data. Analysis of Fourier difference maps worked well for NXMEM since regions of atomic density are well separated from noise regions (Hofmann *et al.*, 2007). Nevertheless, it leaves something to be desired. The method inherently relies on the selected crystal plane(s). To claim universal validity, all possible planes should be taken into account. Therefore the method needs to be automatized to work on the three-dimensional density. As good praxis to guard against misinterpretation of the data, one should always scrutinize the (NX)MEM density over a wide range of χ^2.

Looking at NXMEM calculations for $Ba_8Ga_{16}Sn_{30}$, we note the striking decrease in the value of the optimum χ^2 as we go from the full data set to low resolution for both the simulated and experimental data (Figs. 7 and 8). The simulated case allowed a comparison of the true and approximate $F^{\rm eNDD}$, revealing that the increased χ^2 could be traced to only two of 1102 (100 K) and 927 (300 K) observed reflections which were incorrectly deconvoluted by the simplistic refinement model. This, however, did not affect the NXMEM solution beyond raising the optimum χ^2.

The limits for NXMEM applications should be explored in the future. It is likely to be challenged by crystal systems where atomic form factors have substantially different angular dependences. So far, NXMEM has only been tested for centric structures, but we expect it to be equally applicable to acentric structures. Since NXMEM is based on the IAM approximation, it will experience difficulties when faced with covalent interactions in compounds consisting of light elements. One remedy for this problem could be to introduce scattering factors based on Hirshfeld atoms (Hirshfeld, 1977).

Several possibilities exist to improve the quality of the NXMEM solutions beyond the current work. (i) The extraction of structure-factor amplitudes from powder data, phase determination, and the estimation of deconvolution factors inherently contain errors due to the approximate structural model. Therefore, both may be enhanced by improving the model based on *e.g.* an initial NXMEM calculation with a minimally biased model (see the supporting information for an example with PbTe). (ii) The quality of MEM and NXMEM reconstructions can, furthermore, be ameliorated by applying static weighting schemes (de Vries *et al.*, 1994; Iversen *et al.*, 1995) or a higher order of the *F* and *G* constraint (Palatinus & van Smaalen, 2002). (iii) Selecting proper *G* constraints is always a matter of balancing between data scarcity and model bias and can thus be improved.

We envisage a number of future applications and developments of NXMEM. This method promotes the inference of nuclear information from low-resolution data owing to the reduction of solution space. For both data collected on laboratory diffractometers and in diamond anvil cells $\sin(\theta)/\lambda_{\rm max}$ are severely limited. Hence, it could clearly be

advantageous to apply NXMEM in such cases. Besides the characterization of localized disorder effects, NXMEM could also augment the study of highly complex systems such as zeolites and proteins, which are typically limited by poor atomic resolution (Gramm *et al.*, 2006; Ban *et al.*, 2000). In such instances, NXMEM could contribute to the identification of unresolved atoms. In a similar manner, it may also address the inherent MEM issue of density shoulders occurring in situations where a light scatterer is bonded to a much heavier atom (Hofmann *et al.*, 2007).

NXMEM performs deconvolution as a separate step in its present version, but it can potentially be fully incorporated into MEM software. It requires multiple channels, one for each atomic species. Each channel contains a partial NDD, $\rho_j^{\rm NDD}(\mathbf{r})$, which by Fourier transformation leads to partial nuclear structure factors, $F_j^{\rm NDD}(\mathbf{H})$. The total EDD structure factors are calculated from these by $F^{\rm EDD} = \sum_j f_j F_j^{\rm NDD}$. Such an integrated method would address the problems of inaccurate deconvolution factors, which are inherent to the current NXMEM procedure. Two-channel methods have already been implemented for neutron scattering, spin densities and deformation densities (Papoular & Gillon, 1990; Papoular *et al.*, 1996). For the best possible performance, NXMEM should be integrated with MEM-based pattern fitting (Izumi, 2004).

6. Conclusion

In summary, we have introduced NXMEM (nuclear-weighted X-ray maximum entropy method) as a novel method for reconstructing electron-weighted nuclear density distributions from X-ray data. As proof of concept, we have applied NXMEM to simulated powder X-ray diffraction (PXRD) of PbTe and simulated and experimental single-crystal X-ray diffraction (SCXRD) of $Ba_8Ga_{16}Sn_{30}$. NXMEM proved to be superior to MEM in recovering quantitative information about the intriguing disorder occurring at the Pb and Ba sites.

For simulated PbTe PXRD data at 100 K, the smallest resolvable displacement is 0.19 Å using the NXMEM approach. The calculated centre-of-charge is a stable measure of the atomic displacement, deviating merely 0.57% from the true value. In contrast, MEM can only resolve displacements down to 0.26 Å with an error of 47% on the centre-of-charge.

The analysis on the $Ba_8Ga_{16}Sn_{30}$ data demonstrates that even for complex structures NXMEM does not introduce artefacts in the ordered part of the structure. If the full resolution of the simulated data sets is included, both MEM and NXMEM successfully resolve the Ba2 disorder. However, the advantages of NXMEM become substantial if only low-resolution data are available. Overall, NXMEM determines the Ba displacement within 6% and is consistently more accurate than MEM. In the applications on the full experimental data set, only NXMEM is able to resolve the Ba2 disorder at the highest temperature of 300 K.

Further work is needed to validate NXMEM on acentric and more complex structures; nonetheless, the present study has established its usefulness in analysing fine disorder in centric structures. NXMEM is in its infancy and has likely not reached its final formulation. For example, to reach its full potential, the deconvolution step needs to be directly implemented in MEM software.

This study emphasizes that essential disorder may be hidden in MEM-determined electron-density distributions. The discovery of localized disorder effects in crystal structures, erroneously believed to be of an ordered nature, has been especially important to the field of thermoelectrics. This has clarified the fundamental origin of the low thermal conductivity in clathrates, lead chalcogenides and Zn_3Sb_4 (Christensen *et al.*, 2010; Bozin *et al.*, 2010; Kastbjerg *et al.*, 2013; Snyder *et al.*, 2004). Generally, the enhanced nuclear resolution obtained by NXMEM widens the temperature range for studying exciting disorder effects and, moreover, reduces the requirement for high-resolution data.

This work was supported by the Danish National Research Foundation (Center for Materials Crystallography, DNRF93).

References

Ban, N., Nissen, P., Hansen, J., Moore, P. B. & Steitz, T. A. (2000). *Science*, **289**, 905–920.
Bentien, A., Iversen, B. B., Bryan, J. D., Stucky, G. D., Palmqvist, A. E. C., Schultz, A. J. & Henning, R. W. (2002). *J. Appl. Phys.* **91**, 5694–5699.
Bentien, A., Palmqvist, A. E. C., Bryan, D., Latturner, S., Stucky, G. D., Furenlid, L. & Iversen, B. B. (2000). *Angew. Chem. Int. Ed.* **40**, 1262–1265.
Bindzus, N. & Iversen, B. B. (2012). *Acta Cryst.* A**68**, 750–762.
Bozin, E. S., Malliakas, C. D., Souvatzis, P., Proffen, T., Spaldin, N. A., Kanatzidis, M. G. & Billinge, S. J. L. (2010). *Science*, **330**, 1660–1663.
Cargnoni, F., Nishibori, E., Rabiller, P., Bertini, L., Snyder, G. J., Christensen, M., Gatti, C. & Iversen, B. B. (2004). *Chem. Eur. J.* **10**, 3861–3870.
Christensen, M., Johnsen, S. & Iversen, B. B. (2010). *Dalton Trans.* **39**, 978–992.
Christensen, M., Lock, N., Overgaard, J. & Iversen, B. B. (2006). *J. Am. Chem. Soc.* **128**, 15657–15665.
Christensen, S., Avila, M. A., Suekuni, K., Piltz, R., Takabatake, T. & Christensen, M. (2013). *Dalton Trans.* **42**, 14766.
Collins, D. M. (1982). *Nature (London)*, **298**, 49–51.
Egami, T. & Billinge, S. J. L. (2003). *Underneath the Bragg Peaks: Structural Analysis of Complex Materials.* Oxford, Boston: Pergamon.
Giacovazzo, C. (2002). *Fundamentals of Crystallography.* Oxford University Press.
Gramm, F., Baerlocher, C., McCusker, L. B., Warrender, S. J., Wright, P. A., Han, B., Hong, S. B., Liu, Z., Ohsuna, T. & Terasaki, O. (2006). *Nature (London)*, **444**, 79–81.
Hauptman, H. (1986). *Science*, **233**, 178–183.
Hirshfeld, F. L. (1977). *Isr. J. Chem.* **16**, 226–229.
Hofmann, A., Netzel, J. & van Smaalen, S. (2007). *Acta Cryst.* B**63**, 285–295.
Iversen, B. B., Nielsen, S. K. & Larsen, F. K. (1995). *Philos. Mag. A*, **72**, 1357–1380.
Izumi, F. (2004). *Solid State Ionics*, **172**, 1–6.
Kastbjerg, S., Bindzus, N., Søndergaard, M., Johnsen, S., Lock, N., Christensen, M., Takata, M., Spackman, M. A. & Brummerstedt Iversen, B. (2013). *Adv. Funct. Mater.* **23**, 5477–5483.
Keiber, T., Bridges, F. & Sales, B. C. (2013). *Phys. Rev. Lett.* **111**, 095504.
Knox, K. R., Bozin, E. S., Malliakas, C. D., Kanatzidis, M. G. & Billinge, S. J. L. (2014). *Phys. Rev. B*, **89**, 014102.

Mathworks (2010). *MATLAB R2010b*.
Nishimura, S., Kobayashi, G., Ohoyama, K., Kanno, R., Yashima, M. & Yamada, A. (2008). *Nat. Mater.* **7**, 707–711.
Nolas, G. S., Cohn, J. L., Slack, G. A. & Schujman, S. B. (1998). *Appl. Phys. Lett.* **73**, 178–180.
Palatinus, L., Prathapa, S. J. & van Smaalen, S. (2012). *J. Appl. Cryst.* **45**, 575–580.
Palatinus, L. & van Smaalen, S. (2002). *Acta Cryst.* A**58**, 559–567.
Papoular, R. J. & Gillon, B. (1990). *Europhys. Lett.* **13**, 429–434.
Papoular, R. J., Vekhter, Y. & Coppens, P. (1996). *Acta Cryst.* A**52**, 397–407.
Patterson, A. L. (1935). *Z. Kristallogr.* **90**, 517–542.
Petříček, V., Dušek, M. & Palatinus, L. (2014). *Z. Kristallogr.* **299**, 345–352.
Sakata, M., Mori, R., Kumazawza, S., Takata, M. & Toraya, H. (1990). *J. Appl. Cryst.* **23**, 526–534.
Sakata, M. & Sato, M. (1990). *Acta Cryst.* A**46**, 263–270.
Sales, B. C., Chakoumakos, B. C., Jin, R., Thompson, J. R. & Mandrus, D. (2001). *Phys. Rev. B*, **63**, 245113.
Smaalen, S. van, Palatinus, L. & Schneider, M. (2003). *Acta Cryst.* A**59**, 459–469.
Snyder, G. J., Christensen, M., Nishibori, E., Caillat, T. & Iversen, B. B. (2004). *Nat. Mater.* **3**, 458–463.
Takata, M., Sakata, M., Kumazawa, S., Larsen, F. K. & Iversen, B. B. (1994). *Acta Cryst.* A**50**, 330–337.
Tanaka, H., Kuroiwa, Y. & Takata, M. (2006). *Phys. Rev. B*, **74**, 172105.
Vries, R. Y. de, Briels, W. J. & Feil, D. (1994). *Acta Cryst.* A**50**, 383–391.
Warren, B. E., Krutter, H. & Morningstar, O. (1936). *J. Am. Ceram. Soc.* **19**, 202–206.
Zhang, Y., Ke, X. Z., Kent, P. R. C., Yang, J. H. & Chen, C. F. (2011). *Phys. Rev. Lett.* **107**, 175503.